Proceedings of the ASME 2010 3rd Joint US-European Fluids Engineering Summer Meeting and 8th International Conference on Nanochannels, Microchannels, and Minichannels
FEDSM-ICNMM2010
August 1-5, 2010, Montreal, Canada

FEDSM-ICNMM2010-30657

POD-BASED ESTIMATIONS OF THE FLOWFIELD FROM PIV WALL GRADIENT MEASUREMENTS IN THE BACKWARD-FACING STEP FLOW

Thien Duy Nguyen[*], **John Craig Wells**
Dept. of Civil & Environmental Engineering
Ritsumeikan University
Kusatsu, Shiga, 525-8577 Japan
gr044050@ed.ritsumei.ac.jp
jwells@se.ritsumei.ac.jp

Paritosh Mokhasi
Wolfram Research Inc
Urbana, IL, 61820-6858 United States
mokhpar@iit.edu

Dietmar Rempfer
Dept. of Mechanical & Aerospace Engineering
Illinois Institute of Technology
Chicago, IL, 60616 United States
rempfer@iit.edu

ABSTRACT

In this paper, particle image velocimetry (PIV) results from a backward-facing step flow, of which Reynolds number is 2800 *based on free stream velocity and step height ($h = 16.5$ mm), are used to demonstrate the capability of proper orthogonal decomposition (POD)-based estimation models. Three-component PIV velocity fields are decomposed into a set of spatial basis functions and a set of temporal coefficients. The estimation models are built to relate the low-order POD coefficients, determined from an ensemble of* 1050 *PIV fields by the "snapshot" method, and the time-resolved wall gradients, measured by a near-wall measurement technique called stereo interfacial PIV. These models are evaluated in terms of reconstruction and prediction of the low-order temporal POD coefficients of the velocity fields. In order to determine the coefficients of the estimation models, linear stochastic estimation (LSE), quadratic stochastic estimation (QSE), principal component regression (PCR) and kernel ridge regression (KRR) are applied. In addition, we introduce a possibility of multi-time POD-based estimations in which past and future information of the wall gradient events is used separately or combined. The results show that the multi-time estimation approaches can improve the prediction process. Among these approaches, the proposed multi-time KRR-POD estimation with optimized time duration of wall gradient information in the past yields the best prediction.*

INTRODUCTION

Separated flows are often important in many engineering applications such as flow over wings, or dunes in rivers, in combustors, turbines and compressors. Many studies have been carried in the field of separated flows to provide a better understanding about the dominant flow structures.

For this purpose, extensive work has been contributed to the backward-facing step (BFS), a well-known, simple geometry of separated flows. In this flow configuration, a recirculation zone is formed under the shear layer that develops at the step and reattaches downstream. Previous investigations have described the statistical characteristics of the flow using single point measurement techniques such as hot wires, surface pressure sensors, laser doppler anemometry (LDA), or the field measurement technique of particle image velocimetry (PIV) ([1–3]).

There has been an increased interest to estimate velocity fields using point measurements, usually pressure. Several researchers have investigated the relationship between the flow structure and surface pressure by applying stochastic estimation [4–8]. Some notable estimation techniques are linear stochastic estimation (LSE) [9, 10], quadratic stochastic estimation (QSE) [6, 7], principal component regression (PCR) and kernel ridge regression (KRR) [8].

As an alternative to direct estimation techniques, several researchers have explored the possibility of LSE, QSE, PCR and KRR techniques to estimate the POD coefficients of velocity

[*]Address all correspondence to this author.

Copyright © 2010 by ASME

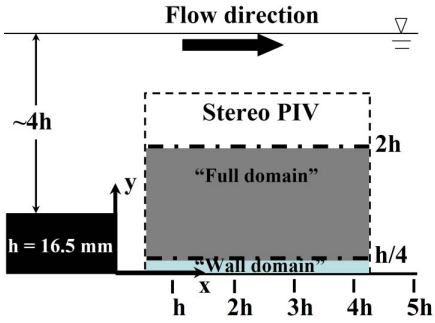

FIGURE 1. BACKWARD-FACING STEP EXPERIMENT.

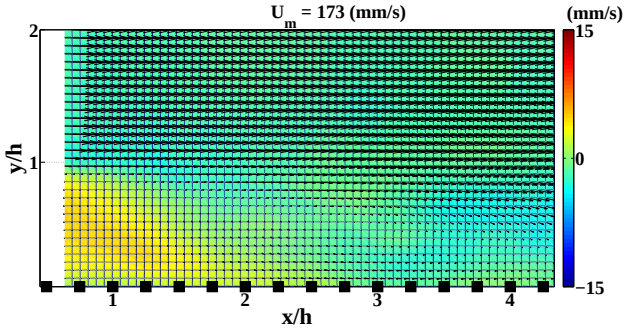

FIGURE 2. MEAN VELOCITY OF THE BACKWARD-FACING STEP FLOW. VECTORS (×3) ARE MEAN STREAMWISE U AND VERTICAL V VELOCITY COMPONENTS, COLOUR SHOWS MEAN SPANWISE VELOCITY COMPONENT W. LOCATIONS OF WALL GRADIENT MEASUREMENTS ARE SHOWN BY BLACK SQUARES.

field given pressure events [6, 8, 10]. In this study, we refer to such approaches as LSE-POD, QSE-POD, PCR-POD and KRR-POD. In order to investigate the capability of estimation models, a common approach is to divide available data into two sets; the estimation model is built by using the first, "training" set, then validated by testing on the second set. The application of an estimation model on the first and second data sets yields "reconstruction" and "prediction" respectively. As examples, Durgesh and Naughton have investigated the performance of LSE-POD to the prediction of wake flow [10], while Mokhasi et al [8] have evaluated the performance of PCR-POD and KRR-POD to predict the numerically simulated 3D flow over a cube.

In this communication, experiments of turbulent flow over a backward-facing step in an open water channel are presented. A stereo-PIV system captures the recirculating flow region behind the step in a laser sheet at the central, vertical plane. The three component PIV velocity fields of 2100 snapshots are decomposed into a set of spatial basis functions and a set of temporal coefficients by the snapshot POD. Unlike previous work, which uses pressure measurements, the inputs to our estimation models are the spatial distributions of wall shear gradient, measured simultaneously by our near-wall measurement technique "stereo interfacial PIV" [11]. In this study, we employ various POD-based estimation techniques, LSE-POD, QSE-POD, PCR-POD and KRR-POD, to estimate the low-order POD coefficients. We take special care to evaluate the estimation models for the accuracy of both reconstruction and prediction. In addition to such single-time estimations, we evaluate the performance of the multi-time LSE-POD estimation [10] and as another innovation introduce and test multi-time PCR-POD and KRR-POD estimations, in which past and/or future wall gradient data is used. Finally, we compare the accuracy of these single-time and multi-time estimation models for reconstruction and prediction of the low-order POD coefficients of the velocity fields.

EXPERIMENT

The experiment setup is sketched in fig. 1. Experiment with a backward-facing step was conducted in an 8 m × 0.5 m (length × width) open water channel. The Reynolds number Re_h based on the mean streamwise velocity U_m and the step height H ($H = 16.5$ mm) was about 2800. The coordinate origin was at the step corner with the streamwise, vertical and spanwise directions denoted by x, y and z respectively. Hollow glass sphere particles with a mean diameter of 10 μm seeded the water flow. A double pulsed Nd:YAG laser illuminated a 2 mm thick vertical sheet of the flow in the mid-plane of the test section. The fluid region in the xy plane, with x/h ranging from 0.5 to 4.25, was imaged by a stereo PIV system comprised of two Kodak Megaplus Model ES1.0 charge couple device (CCD) cameras with resolutions of 1018×1008 pixels. In the stereo configuration, cameras viewed horizontally at 45 degrees from downstream on either side of the channel, viewing through the water prisms on the sidewalls. The camera bodies were slightly rotated to satisfy the Scheimpflug condition. Acquisition software was adapted in the LabView platform to control a PCI NI-6601 timer board for generating external triggers. A total of 2100 PIV image pairs corresponding to six experimental runs were acquired. The time interval between the first and second exposures was $\triangle t = 3$ ms and sampling rate was set at 15 Hz.

The PIV images were processed by a standard cross-correlation algorithm. The size of the interrogation window was about 33×33 pixels, equivalent to 2×2 mm^2, with 50% overlap. This resulted in a vector spacing of 1 mm. The seeding density was about eight to ten particles per interrogation area. In the velocity computation, vectors conflicting with the local median criterion were replaced by that corresponding to the second highest peak in correlation map. The mean three-component velocity of backward-facing step flow is shown in fig. 2. The color shows the mean spanwise velocity component, of which maximal magnitude is about 3% of the mean bulk velocity U_m which is defined as $U_m = Q_f/A_f$, where A_f is cross-sectioned area upstream of the

Copyright © 2010 by ASME

step, and Q_f is the bulk flow rate.

The two components of wall shear gradient, $\partial u/\partial y$ and $\partial w/\partial y$, were obtained by applying our near-wall measurement technique, stereo-IPIV [11], to the set of experimental images as follows. For PIV images captured by each of the oblique camera views, we firstly identified the wall boundary. Second, the image segment above the wall was mapped to the rectangle by means of the image transformation. The lower edge of such image template coincided with the wall boundary. Third, we calculated the stack of 1D correlation curves by cross-correlating each horizontal pixel line within the templates of the transformed images of the first and second exposures. Fourth, the wall shear gradient was determined by fitting the straight line into the correlation stack; and searched for the corresponding slope which maximized the Gaussian-weighted sum of correlation values. Fifth, the projected wall shear gradient was obtained by the reverse transformation. Finally, we performed the stereo-reconstruction to achieve two components of wall shear gradient, $\partial u/\partial y$ and $\partial w/\partial y$. In our BFS application, the wall gradient measurement was performed at 16 locations along the streamwise direction, at a spacing of $0.25h$ ranging from $0.5h$ to $4.25h$. The locations of wall gradient measurements are shown by the black squares in fig. 2. In previous work [11], this technique has proven to provide a better accuracy of wall gradient measurement in comparison with differentiating velocity vector derived from standard PIV processing technique such as particle image distortion [12].

POD analysis is performed on the measured velocity fields and wall shear measurements in order to extract the statistically dominant structures in the flow and wall shear. In the next section, a brief review of POD technique and results from the BFS flow decomposition will be presented.

PROPER ORTHOGONAL DECOMPOSITION

The Karhunen-Loeve decomposition, or proper orthogonal decomposition (POD) technique has been an effective tool to identify dominant flow features by performing decomposition to the experimental and numerical data. Lumley first applied POD to identify the large-scale structures in turbulent flows [14]. Mathematical details of direct POD method can be found in many references [15, 16] but a brief review is provided here. The decomposition of a velocity field ***u(x,t)*** is given by

$$\boldsymbol{u}(\boldsymbol{x},t) = \sum_{k=1}^{N} \zeta_k(t)\psi_k(\boldsymbol{x}), \tag{1}$$

where $\zeta_k(t)$ are called the temporal POD coefficients and $\psi(\boldsymbol{x})$ are called the POD basis functions which are the eigenfunctions

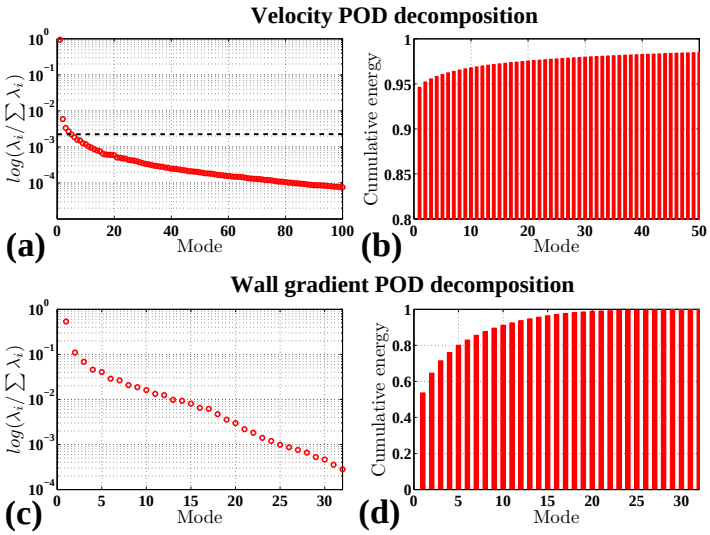

FIGURE 3. (a) ENERGY SPECTRA, (b) CUMULATIVE ENERGY FROM FULL DOMAIN VELOCITY POD DECOMPOSITION; (c) ENERGY SPECTRA, (d) CUMULATIVE ENERGY FROM WALL GRADIENT POD DECOMPOSITION. THE DASHED LINE IN (a) INDICATES THE EPPS & TECHET [13] THRESHOLD FOR THE POD EIGENVALUES.

of the two-point correlation function $R(\boldsymbol{x},\boldsymbol{x}')$ defined as

$$R(\boldsymbol{x},\boldsymbol{x}') = \frac{1}{T}\int \boldsymbol{u}(\boldsymbol{x},t)\cdot\boldsymbol{u}(\boldsymbol{x}',t)dt. \tag{2}$$

The basis functions are computed via an optimization problem leading to a Fredholm integral equation

$$\int R(\boldsymbol{x},\boldsymbol{x}')\cdot\psi(\boldsymbol{x}')d\boldsymbol{x}' = \lambda\,\psi(\boldsymbol{x}). \tag{3}$$

The eigenvalue λ associated with each POD mode represents the kinetic energy contained in that mode. The decomposition yields statistically dominant flow structures in the few lowest-order POD modes, which capture most of the flow kinetic energy. Since the experimental results obtained by PIV measurements are discrete, the integrals are computed by discrete summations. In this case, the snapshot POD developed by Sirovich and Kirby [17] is usually more computationally efficient. A correlation matrix is calculated as

$$C_{ij} = \frac{1}{N}\int \boldsymbol{u}(\boldsymbol{x},t_i)\cdot\boldsymbol{u}(\boldsymbol{x},t_j)d\boldsymbol{x}, \tag{4}$$

where N is the number of PIV velocity snapshots. In order to compute the POD basis functions and temporal coefficients, let

Copyright © 2010 by ASME

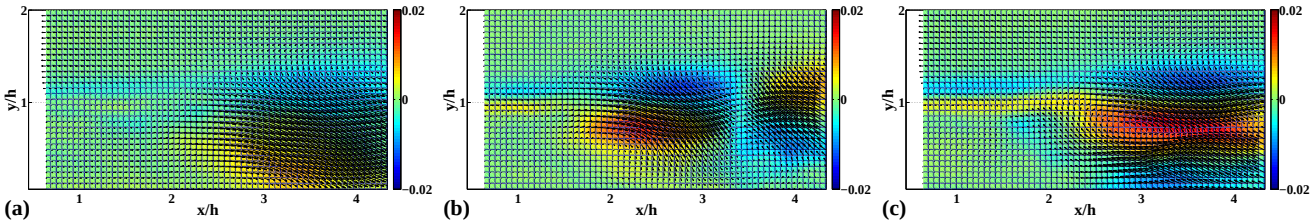

FIGURE 4. LOW-ORDER POD VELOCITY MODES (×3), (a) MODE 2, (b) MODE 3, (c) MODE 4. COLOUR SHOWS VORTICITY CALCULATED FROM CORRESPONDING VELOCITY MODE.

us first define α_{ki} as

$$\alpha_{ki} = \frac{\upsilon_i^k}{\sqrt{N\sum_{m=1}^{N}\sum_{r=1}^{N}\upsilon_m^k\upsilon_r^k C_{mr}}} \tag{5}$$

where υ_i^k is the ith element of the eigenvector υ^k corresponding to the eigenvalue λ_k of the correlation matrix $\boldsymbol{C}$. The POD basis functions are then computed as

$$\psi_k(\boldsymbol{x}) = \sum_{i=1}^{N}\alpha_{ki}\boldsymbol{u}(\boldsymbol{x},t_i), \tag{6}$$

and the temporal coefficients as

$$\zeta_k(t_p) = \int \boldsymbol{u}(\boldsymbol{x},t_p)\cdot\psi_k(\boldsymbol{x})d\boldsymbol{x} = N\sum_{i=1}^{N}\alpha_{ki}C_{ip}. \tag{7}$$

The eigenvectors and temporal coefficients of the POD decomposition satisfy the following orthogonality:

$$\int \psi_i(\boldsymbol{x})\cdot\psi_j(\boldsymbol{x})d\boldsymbol{x} = \delta_{ij}, \tag{8}$$

$$\frac{1}{T}\int_0^T \zeta_i(t)\zeta_j(t)dt = \lambda_i\delta_{ij}. \tag{9}$$

The present PIV setup allows us to capture several hundreds to a few thousand instantaneous three component velocity fields. The volume of these PIV measurements sufficies for a POD analysis to reveal the statistically dominant structures of the flow. In addition to the three-component velocity fields, a strictly analogous POD of wall shear gradients obtained from stereo PIV is performed.

Figure 3a, b show the energy spectra and cumulative energy of the velocity decomposition. The energy fraction of the first POD mode, which is approximately equal to the averaged flow, is found to contribute 94% of the total energy of the flow. This contribution is identical to the energy fraction of the mean flow found for the BFS flow in [18]. Compared to results from numerical simulations, there are many experimental sources of error that may dominate the representation of high-order modes, include low seeding density, high velocity gradients, out of plane particle motion [19], inhomogeneous laser intensity, and precision of camera calibration. Comparing the POD modes obtained from experiments and direct numerical simulation of a cylinder wake flow, Ma et al [20] found that the experimental modes above the fifth POD mode were contaminated by noise. In this work, we retain only the first four POD modes, which contain about 96% of the total energy of the flow, consistent with the following threshold criterion for the magnitude λ_k of retained POD modes extracted from PIV data [13],

$$\lambda_k > \sqrt{ND}\varepsilon, \tag{10}$$

where N is the number of snapshots, D is the number of spatial points in the PIV vector field and ε is the uncertainty of velocity measurement which, according to [19], corresponds to a root mean square error of approximately $\varepsilon = 0.1\ (pixel/\triangle t)$. In this application, $\varepsilon = 2.5\ (mm/s)$ (about 2% of the mean flow), $N = 2100$ and $D = 2046$ yield $\lambda_k \approx 5200\ (mm/s)$. The dashed line in fig. 3a indicates the Epps and Techet's threshold for the POD eigenvalues. Figure 4 shows the in-plane components of the low-order POD modes ($k = 2$, 3 and 4) overplotted on the corresponding vorticity modes. To get a more quantitative idea of low-order POD modes reconstruction, fig. 6 shows the reconstructions of Reynolds stress distributions using the first four POD modes. Compared to those distributions obtained from the original PIV measurements (fig. 5), the low-order modes (i.e. large-scale structures) appear to be responsible for the majority of the background stress levels. However, the percent contribution of these large scales to the reconstructed distributions is different for each Reynolds stress component. The $\langle -uv\rangle$ Reynolds stress distribution is the best reconstructed, with a recovery of 86% of the original peak stress level. The corresponding values are 77% for the maximal value of the u_{rms} Reynolds stress component, and 64% for the v_{rms} stress component. These reconstructed

Copyright © 2010 by ASME

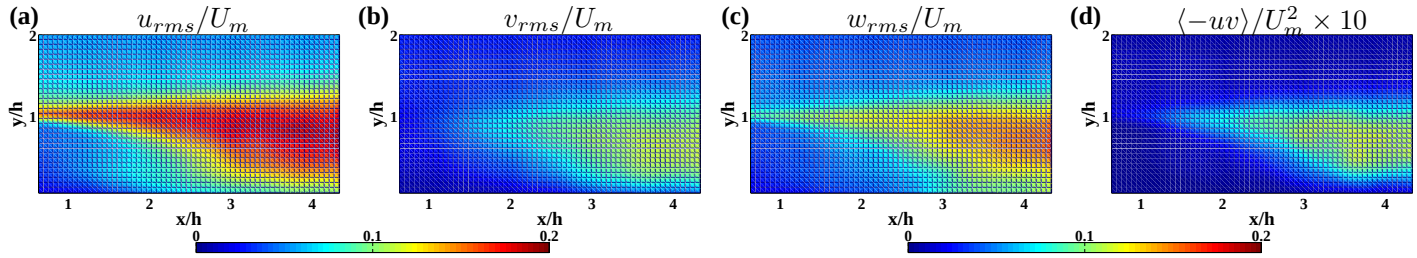

FIGURE 5. (a) u_{rms}/U_m, (b) v_{rms}/U_m, (c) w_{rms}/U_m, (d) $\langle -uv \rangle / U_m^2 \times 10$ CALCULATED FROM THE ORIGINAL VELOCITY FIELDS.

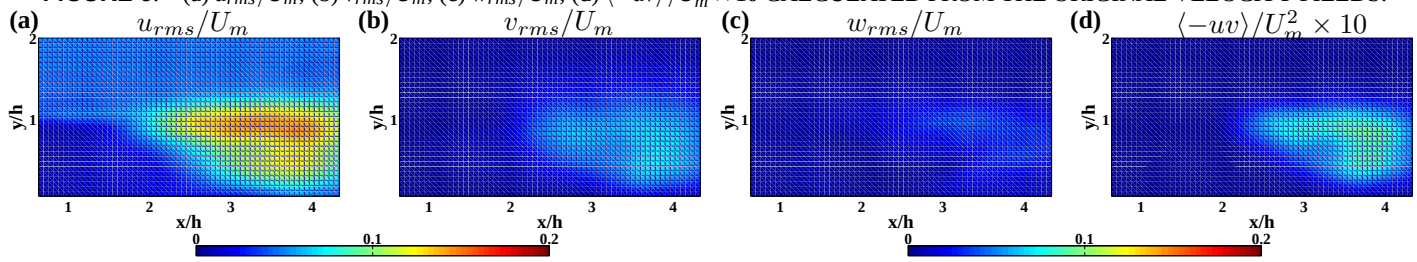

FIGURE 6. (a) u_{rms}/U_m, (b) v_{rms}/U_m, (c) w_{rms}/U_m, (d) $\langle -uv \rangle / U_m^2 \times 10$ CALCULATED FROM THE VELOCITY FIELDS RECONSTRUCTED BY 4 POD MODES.

stress levels are close to those recovered from using the first five POD modes in [18] for BFS flow. Compared to the low-order mode reconstructions of the u_{rms}, v_{rms} and $\langle -uv \rangle$ stress components, only a small fraction of the maximal stress level of w_{rms} is recovered, i.e. 27%. This result indicates that the cross-stream motion is less well reconstructed by the low-order POD modes because they are associated with higher-order structures which are not included in our truncation [21].

Figure 3c, d show the energy spectra and cumulative energy of the wall gradient decomposition. The first four spatial functions of the POD wall gradient decomposition for $\partial u/\partial y$ and $\partial w/\partial y$ are shown in fig. 7. The modal descriptions of the $\partial u/\partial y$ and $\partial w/\partial y$ components indicate that the given flow is three-dimensional and complex, especially at the region near the reattachment point $X_r = 5.5h$ found in [11].

POD-BASED ESTIMATION APPROACH

In this section, we describe various POD-based estimation approaches, including single-time and multi-time estimations, used to build estimation models. The moderately sparse wall gradients measured by stereo-IPIV and temporal POD coefficients of velocity fields are related by measurement models which then can be used to estimate the flow from wall shear data.

Single-time LSE-POD and QSE-POD

The stochastic estimation approach, introduced by Adrian [22], predicts a time-dependent signal given a correlated measurement event. In [23], the authors proposed to use stochastic estimation to approximate the conditional averages of turbulent flow parameters associated with unconditional data.

For this application, the temporal POD coefficients of velocity fields are estimated by a conditional average associated with the wall shear gradient denoted by $\boldsymbol{s}(t)$. This can be described as

$$\tilde{\zeta}_k(t) = \langle \zeta_k(t) \mid \boldsymbol{s}(t) \rangle , \tag{11}$$

where the subscript k denotes the POD mode and the angle brackets $\langle . \rangle$ denote the ensemble averaging. The conditional average can be approximated by a truncated power series expansion [24] which, in QSE-POD, is truncated at the quadratic terms,

$$\tilde{\zeta}_k(t) = \sum_{m=1}^{M} A_{km} \boldsymbol{s}_{km}(t) + \sum_{m=1}^{M} \sum_{n=1}^{M} B_{kmn} \boldsymbol{s}_m(t) \boldsymbol{s}_n(t). \tag{12}$$

while in LSE-POD it is truncated at the linear term. The summation covers wall gradient measurement locations indicated by m.

In the present communication, both the linear and quadratic stochastic estimations are applied to the wall gradient events. To derive these estimation coefficients, the process of minimizing the mean-square error is performed by taking derivatives with respect to A and B, then setting these expressions to zero. This procedure yields a linear system of equations that describes the coefficients A and B in terms of wall gradient autocorrelations $[\boldsymbol{SS}]$ and POD coefficient-wall gradient correlations $[\zeta \boldsymbol{S}]$

$$[AB] = [\boldsymbol{SS}]^{-1} [\zeta \boldsymbol{S}] . \tag{13}$$

Copyright © 2010 by ASME

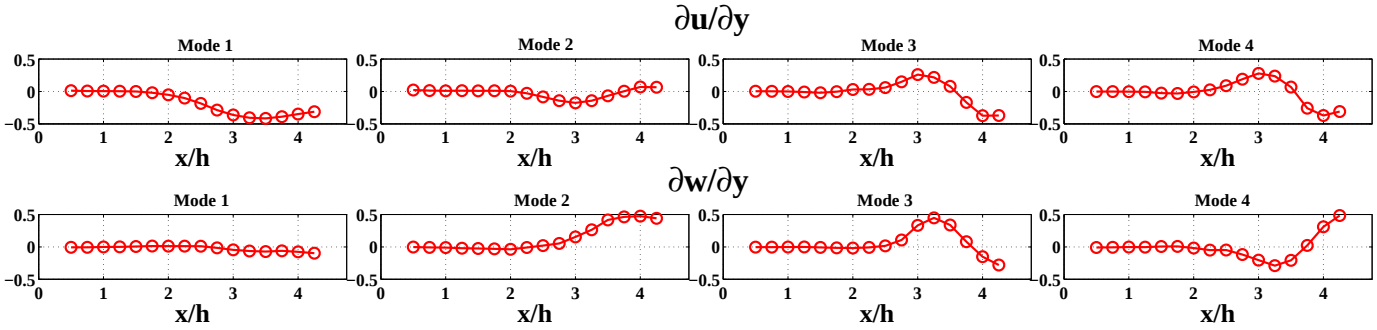

FIGURE 7. LOW-ORDER POD MODES OF WALL GRADIENTS, TOP: $\frac{\partial u}{\partial y}$, BOTTOM: $\frac{\partial w}{\partial y}$.

From the decomposition of PIV velocity vector fields and wall gradient results of stereo-IPIV, the correlation matrices on the right hand side can be evaluated to calculate estimation coefficients. Due to the difference of the minimizing process, the coefficients of LSE and the linear coefficients of QSE are not identical.

Single-time PCR-POD and KRR-POD

In addition to the LSE-POD and QSE-POD techniques, we use the principal component regression (PCR) and kernel ridge regression (KRR) that produce linear and nonlinear estimations respectively to determine the estimation models. The PCR-POD and KRR-POD are briefly presented next, following Mokhasi et al [8].

Single-time PCR-POD The single-time PCR-POD technique estimates the POD coefficients $\zeta_k(t)$ through a linear relation with the wall gradient event $\boldsymbol{s}(t)$

$$\tilde{\zeta}_k(t) = \sum_{m=1}^{M} w_{km}\boldsymbol{s}_{km}(t), \tag{14}$$

where M is the number of wall gradient measurement points, and $\boldsymbol{w}$ are the coefficients of the PCR-POD regression need to be determined. It can be seen that the number of PCR-POD estimation coefficients is equal to the number of wall gradient measurement points, M. Analogously to other estimation techniques, the objective of this technique is to minimize the mean-square error function $C(w)$ between the estimated and the true temporal POD coefficients

$$C(w) = min.\frac{1}{2}\sum_{i=1}^{N}\left(\boldsymbol{w}_i\boldsymbol{s}(t_i) - \zeta_i(t)\right)^2, \tag{15}$$

where $\boldsymbol{s}(t_i)$ is the wall gradient event at time t_i from N measurements, $\zeta_i(t)$ is the ith POD coefficient of the velocity fields. Instead of deriving $\boldsymbol{w}$ by conventionally solving the linear system of derivative equation, the PCR-POD technique looks for the coefficients that are the functions of the principal components of the events, wall gradients in our case. Hence, a POD calculation is performed to analyse to the time resolved wall gradient $\boldsymbol{s}$ as below

$$s_r^{EN}(t) = \sum_{m=1}^{N_p}\beta_m^{EN}(t)\Gamma_{mr}^{EN}, \tag{16}$$

where Γ and β with superscript EN are the spatial and temporal eigenfunctions derived from the given ensemble wall gradient events respectively. N_p is the number of modes used in the POD decomposition. In the general terminology of measurement models, N_p is called the number of "latent variables"; its effect on the PCR-POD performance is discussed later. The maximal value of N_p depends on the number of snapshots and the number of spatial measurement points of the wall gradient. The orthogonality of Γ and β can be described as,

$$\beta_m^{EN}(t) = \sum_{r=1}^{N_p} s_r^{EN}(t)\Gamma_{mr}^{EN}, \tag{17}$$

Next, a relationship between the POD coefficients of the velocity fields and the POD coefficients of the wall gradient events is built as

$$\zeta_k(t) = \mathbf{M}_{km}\beta_m(t), \tag{18}$$

by solving the linear equation system expressed in equ. 19

$$\mathbf{M}_{km} = \sum_{s=1}^{N_p}\zeta_{ks}^{EN}\omega_{sm}. \tag{19}$$

Copyright © 2010 by ASME

where

$$\sum_{s=1}^{N_p} \beta_{ms}^{EN} \omega_{sr} = \delta_{mr}. \tag{20}$$

By plugging the equ. 17 and equ. 20 into the equ. 18, one can derive the final form as

$$\zeta_k(t) = \sum_{r=1}^{N_p} \left(\sum_{i=1}^{N_p} \sum_{j=1}^{N_p} \left(\zeta_{ki}^{EN} \omega_{im} \sum_{m=1}^{N_p} \omega_{jm} s_{rj}^{EN} \right) \right) s_r(t). \tag{21}$$

This equation represents a prediction for the temporal POD coefficients $\zeta(t)$ from the given wall gradient $\boldsymbol{s}$ through a linear relation.

Single-time KRR-POD In this application of kernel ridge regression (KRR), POD coefficients $\zeta_k(t)$ are approximated by a nonlinear relationship with wall gradient $\boldsymbol{s}(t)$ shown below:

$$\zeta_k(s) = \sum_{j=1}^{N} w_j^k h_j(s), \tag{22}$$

where N is the number of snapshots, $\boldsymbol{w}^k$ are the estimation coefficients and h_j are nonlinear basis functions, most commonly radial basis functions (RBF). In this application, we use N vector values of wall gradient $\boldsymbol{s}$ to make the regression. Therefore, the number of KRR-POD estimation coefficients for each ζ_k is N. Details of the RBF functions can be found in [8]. In this study, h is chosen to be a multi-quadric function which has the form

$$h_j(s) = \phi(s, s_j) = \sqrt{1 + \varepsilon^2 \left\| s - s_j \right\|_2^2}, \tag{23}$$

where ε is a scaling parameter and $\left\| \boldsymbol{s} - \boldsymbol{s}_j \right\|_2^2$ is the Euclidean distance between the wall gradients $\boldsymbol{s}$ and $\boldsymbol{s}_j$. In the KRR-POD approach, the objective is to minimize a cost function defined as

$$C(\boldsymbol{w}) = \sum_{i=1}^{N} (\zeta_i - \zeta_i(\boldsymbol{s}))^2 + \sum_{j=1}^{N} \beta_j w_j^2, \tag{24}$$

where the regularization parameters β are added to penalize large coefficients $\boldsymbol{w}$ that could appear due to multicollinearity [8]. These parameters need not to constant and are often optimally determined by generalized cross validation or leave-one-out cross validation. In this application, N is rather large, so we set $\beta_j = \beta \forall j$, the unknown coefficients $\boldsymbol{w}$ are computed by taking the derivative of equ. 24 and setting to zero;

$$\frac{\partial C}{\partial w_j^k} = 2 \sum_{i=1}^{N} (\zeta_i(\boldsymbol{s}) - \zeta_i) h_j(\boldsymbol{s}_i) + 2\beta w_j^k = 0. \tag{25}$$

In terms of the RBF functions denoted as

$$H_{ij} = h_j(\boldsymbol{s}_i) = \phi\left(\left\| \boldsymbol{s}_i^{EN} - \boldsymbol{s}_j^{EN} \right\| \right), \tag{26}$$

the coefficient $\boldsymbol{w}$ can be evaluated by solving a system of linear equations. The result written in matrix notation is

$$w_j = \left[H_{ij}^T H_{ij} + \beta I_{ij} \right]^{-1} H_{ij}^T \zeta_j, \tag{27}$$

where I denotes the square identity matrix and the superscript EN indicates that term is from the ensemble. Once the $\boldsymbol{w}$ coefficients are determined, one can substitute $\boldsymbol{w}$ into equ. 22 to find the regression form of KRR-POD technique as

$$\zeta_k(t) = \sum_{j=1}^{N} w_j \phi\left(\left\| s_j^{EN} - s \right\| \right). \tag{28}$$

Like the other estimation techniques applied here, one can estimate the POD coefficients $\zeta(t)$ of the velocity fields from the wall gradient events by using equ. 28.

Multi-time POD-based estimations

In the previously described estimation techniques, the POD coefficients of velocity fields are estimated by using the wall gradient events at a single time. On the other hand, several studies have discussed an extension of LSE-POD approach with multi-time-delay implemented in a frequency domain [25, 26] or in a time domain [10].

In this part, we describe the multi-time estimation LSE-POD, PCR-POD and KRR-POD techniques in which the information of wall gradient events from the past and future is separately used or combined to build the models. In this circumstance, the estimated POD coefficients of the velocity field at time t are expressed in terms of conditional averages by

$$\tilde{\zeta}_k(t) = \left\langle \zeta_k(t) \mid \boldsymbol{s}(t'), t - T \le t' \le t \right\rangle, \tag{29}$$

$$\tilde{\zeta}_k(t) = \left\langle \zeta_k(t) \mid \boldsymbol{s}(t'), t \le t' \le t + T \right\rangle, \tag{30}$$

$$\tilde{\zeta}_k(t) = \left\langle \zeta_k(t) \mid \boldsymbol{s}(t'), t - T \le t' \le t + T \right\rangle, \tag{31}$$

where subscript k denotes the POD mode estimated at time t, T is the duration of the temporal window of wall gradient events used

Copyright © 2010 by ASME

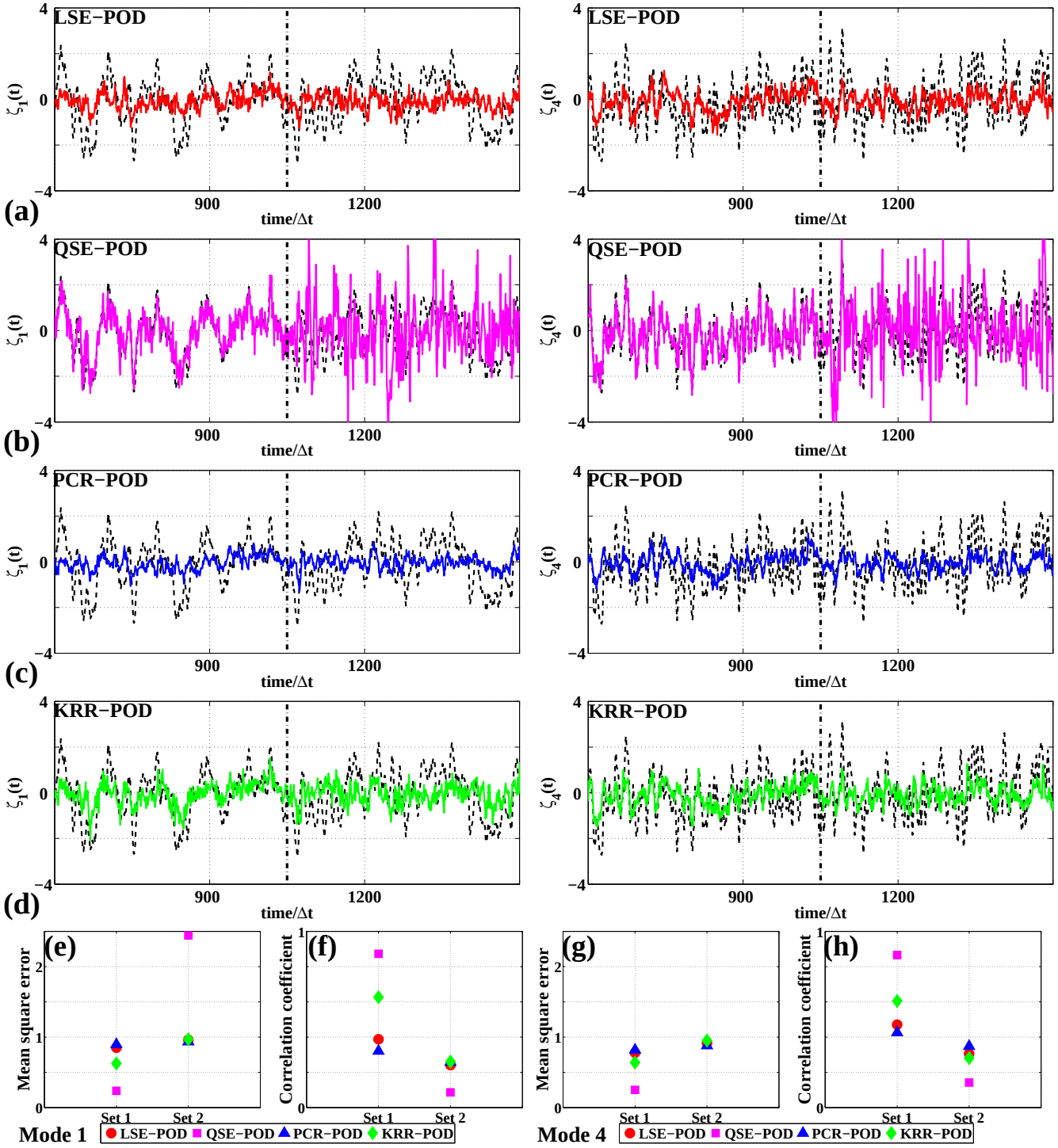

FIGURE 8. RESULTS FROM THE FULL DOMAIN, **a-d** SHOW COMPARISONS BETWEEN THE ACTUAL (DASHED) AND ESTIMATED POD COEFFICIENTS (SOLID) OF MODE 1 AND MODE 4, **e-h** SHOW THE MEAN-SQUARE ERRORS AND CORRELATION COEFFICIENTS OF VELOCITY MODE 1 AND MODE 4. THE DATA SET 2 CORRESPONDING TO $time/\triangle t > 1050$ (INDICATED BY VERTICAL LINE) IS OUTSIDE THE TRAINING ENSEMBLE. THE NUMBER OF LATENT VARIABLES IN PCR-POD AND THE VALUES OF (ε, β) IN KRR-POD ARE SELECTED TO OPTIMIZE THE PREDICTION PROCESS. THE POD COEFFICIENTS ARE STANDARDIZED BY *Z-SCORE* NORMALIZATION.

Copyright © 2010 by ASME

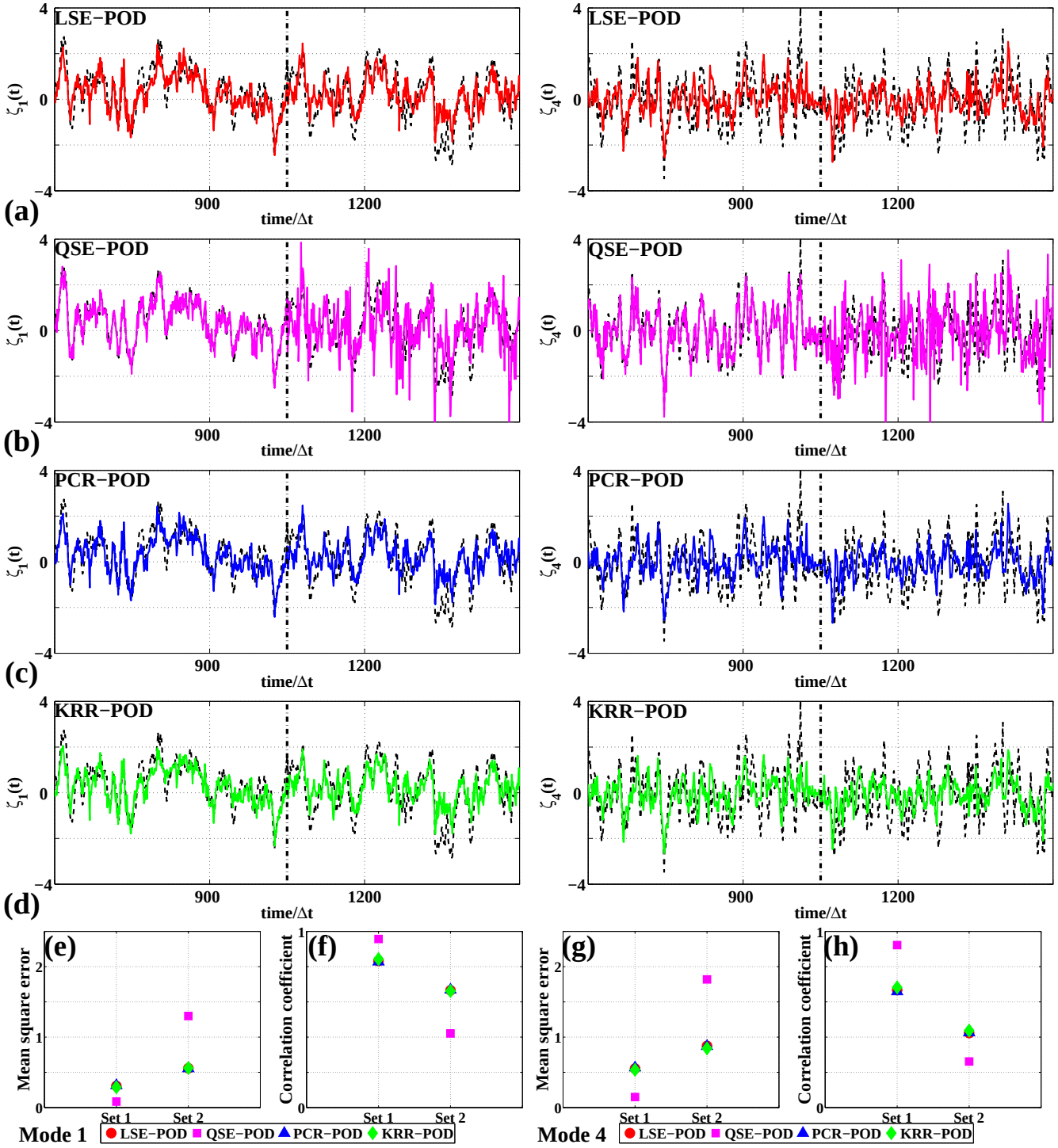

FIGURE 9. RESULTS FROM THE WALL DOMAIN, **a-d** SHOW COMPARISONS BETWEEN THE ACTUAL (DASHED) AND ESTIMATED POD COEFFICIENTS (SOLID) OF MODE 1 AND MODE 4, **e-h** SHOW THE MEAN-SQUARE ERRORS AND CORRELATION COEFFICIENTS OF VELOCITY MODE 1 AND MODE 4. THE DATA SET 2 CORRESPONDING TO $time/\triangle t > 1050$ (INDICATED BY VERTICAL LINE) IS OUTSIDE THE TRAINING ENSEMBLE. THE NUMBER OF LATENT VARIABLE IN PCR-POD AND THE VALUES OF (ε, β) IN KRR-POD ARE SELECTED TO OPTIMIZE THE PREDICTION PROCESS. THE POD COEFFICIENTS ARE STANDARDIZED BY *Z-SCORE* NORMALIZATION.

Copyright © 2010 by ASME

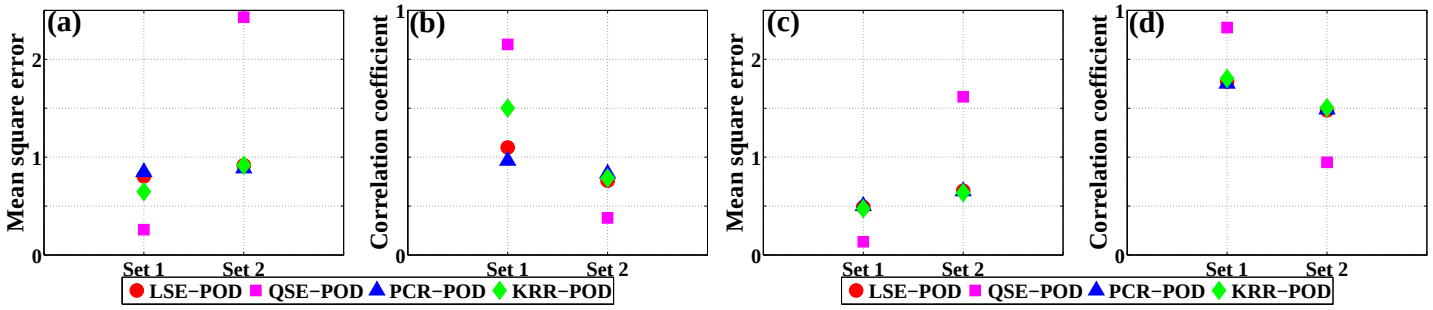

FIGURE 10. MEAN-SQUARE ERRORS AND CORRELATION COEFFICIENTS BETWEEN ACTUAL AND ESTIMATED POD COEFFICIENTS BY SINGLE-TIME LSE-POD, QSE-POD, PCR-POD AND KRR-POD. (a), (b): FROM FULL DOMAIN, (c), (d): FROM WALL DOMAIN.

in the multi-time estimation. Equation 29 and 30 express that past and future information on wall gradients is used separately, while equ. 31 specifies that both past and future information on wall gradients is combined.

In the multi-time LSE-POD estimation, the estimates of POD coefficient are;

$$\tilde{\zeta}_k(t) = \sum_{j=1}^{M} \sum_{i=-I}^{0} A_{k,j}^{i} \boldsymbol{s}_j(t+i\triangle t), \tag{32}$$

$$\tilde{\zeta}_k(t) = \sum_{j=1}^{M} \sum_{i=0}^{I} A_{k,j}^{i} \boldsymbol{s}_j(t+i\triangle t), \tag{33}$$

$$\tilde{\zeta}_k(t) = \sum_{j=1}^{M} \sum_{i=-I}^{I} A_{k,j}^{i} \boldsymbol{s}_j(t+i\triangle t), \tag{34}$$

where M is the number of wall gradient measurement locations, $T = I\triangle t$ is the time duration, and $A_{k,j}^{i}$ is the coefficient of the estimation model. The estimation coefficients are derived by the mean-square error minimizing. This procedure yields a linear system of equations for the estimation coefficients A in terms of wall gradient autocorrelation $[\mathbf{S}_t\mathbf{S}_t]$ and POD coefficient-wall gradient correlation $[\zeta\mathbf{S}_t]$,

$$[A] = [\mathbf{S}_t\mathbf{S}_t]^{-1}[\zeta\mathbf{S}_t]. \tag{35}$$

For the multi-time PCR-POD and KRR-POD estimations, the implementations are similar to the single-time approaches. The only difference is that the matrix of event $\boldsymbol{s}$, as with LSE-POD, is now expanded to include the wall gradients from the past and/or future. Compared to the standard single-time estimations, the number of estimation coefficients of the multi-time LSE-POD and PCR-POD approaches increases in proportion to the increase of the time duration while that of the multi-time KRR-POD is still N.

RESULTS AND DISCUSSION

The estimation techniques discussed in the previous section have been applied to the BFS flow, and their accuracy has been compared via mean-square errors and correlation coefficients between the "true" POD coefficients, determined from the experimental velocity fields by projection onto ψ_k, and their estimated values. Before processing, the POD coefficients are standardized by applying *z-score* normalization, which shifts and re-scales the signal to a mean of zero and a standard deviation of one. As a result, all the normalized POD coefficients have the same standard deviation that gives an unbiased estimation to any POD coefficient [8]. The mean-square errors between the true and estimated POD coefficients, ζ and $\tilde{\zeta}$ respectively, are calculated by

$$\varepsilon^2 = \frac{1}{NN_v} \sum_{t=1}^{N} \sum_{k=1}^{N_v} \left(\tilde{\zeta}_k(t) - \zeta_k(t)\right)^2, \tag{36}$$

where N is the number of snapshots in the data set, N_v is the number of low-order POD coefficients ($N_v = 4$ in our application, or $N_v = 1$ when considering the error of a single mode). The correlation coefficient between the true and estimated POD coefficients, $\zeta_k(t)$ and $\tilde{\zeta}_k(t)$ respectively, are calculated by

$$C_k = \frac{\sum_{t=1}^{N}(\tilde{\zeta}_k(t) - <\tilde{\zeta}_k>)(\zeta_k(t) - <\zeta_k>)}{\sqrt{\sum_{t=1}^{N}\left(\tilde{\zeta}_k(t) - <\tilde{\zeta}_k>\right)^2}\sqrt{\sum_{t=1}^{N}(\zeta_k(t) - <\zeta_k>)^2}}, \tag{37}$$

where k indicates the POD mode, N is the number of snapshots in the data set and the operator $\langle . \rangle$ stands for the ensemble average.

A total of 2100 PIV realizations and their corresponding wall shear gradients have been divided into two sets of 1050 snapshots. In this assessment, we first perform a POD decomposition on the first data set of the velocity fields, called the "ensemble", to obtain the spatial POD basis functions. Next, the time series of the four lowest-order temporal POD coefficients and corresponding wall gradients from the first set are used to build

Copyright © 2010 by ASME

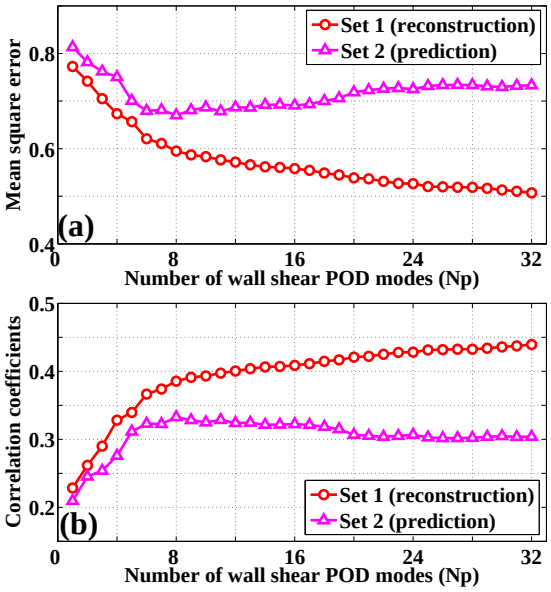

FIGURE 11. FULL DOMAIN: EFFECTS OF THE NUMBER N_p OF LATENT VARIABLES ON PERFORMANCE OF PCR-POD ESTIMATION, (a) MEAN-SQUARE ERROR, (b) CORRELATION COEFFICIENT.

the estimation models and estimation coefficients. By using the estimation coefficients and wall gradient distributions from "set 1", one can partially "reconstruct" the POD coefficients that correspond to that data set. The accuracy of reconstruction is evaluated by comparing the POD coefficients calculated by the estimation models and the original/"true" POD coefficients obtained directly by equ. 7. Next, if the estimation coefficients determined from the ensemble operate on the wall gradients from another data set, say set 2, one can approximately "predict" the values of POD coefficients of set 2. The accuracy of prediction is computed by comparing the POD coefficients, estimated by applying the models to the wall gradient events from set 2, with the actual POD coefficients, which are obtained by projecting the PIV velocity fields of the second set onto the POD basis functions from the first set. Normally, "reconstruction" yields more accurate estimates than "prediction".

Performances of single-time LSE-POD, QSE-POD, PCR-POD and KRR-POD estimations

First, we evaluate the performances of the single-time LSE-POD, QSE-POD, PCR-POD and KRR-POD estimations.

In the linear estimation technique PCR-POD, one must specify the number N_p of "latent variables" indexed by m in equ. 16, which, in this application, is the number of modes used from the POD decomposition of the wall gradient events. When the maximal number of wall gradient POD modes is used, the result of PCR-POD estimation is identical to that by LSE-POD. For prediction, it is advised to use only the few most energetic eigenvectors from the decomposition to achieve a better regression [8]. In other words, rather than using all measured data, one can optimize the number N_p of latent variables used in PCR-POD to improve the prediction process. This is a benefit of PCR-POD versus LSE-POD. Such consideration is very valuable if one uses tens to hundred(s) of sensors or PIV object points. In this study, we chose $N_p = 8$ as will be now explained. We have evaluated the performance of the PCR-POD estimation technique versus the number N_p of latent variables through the calculation of mean-square errors and correlation coefficients from the reconstruction and prediction procedures. The results are plotted in fig. 11. In our BFS application, the two-component wall shear gradients are measured at 16 streamwise locations, so the maximal value of N_p is 32. It is seen that for reconstruction, the highest accuracy is obtained when all the wall gradient POD modes are used. By contrast, the mean-square error of the prediction process takes a minimum when 8 dominant POD eigenvectors, covering about 60% of the total variance of the wall gradient events from set 1, are used. This value of N_p is accordingly selected for the PCR-POD to optimize its predictive capability.

We perform comparative assessments for two different physical domains. The "full domain" covers a region of x/h ranging from 0.5 to 4.25 and y/h ranging from 0.06 to 2; while the "wall domain" has its upper boundary lowered to $y/h = 0.25$ (fig. 1).

For the performances of LSE-POD, QSE-POD, PCR-POD and KRR-POD to the full domain, fig. 8a-d compare the time series of actual and estimated coefficients of the first and the fourth POD modes of the velocity fields. The process of reconstruction corresponds to the left half of the time series, $time/\triangle t < 1050$, while prediction corresponds to the right half. Figure 8e-h show the corresponding mean-square errors and correlation coefficients. It can be seen from fig. 8 and fig. 10a, b that the reconstructions by the nonlinear estimations, QSE-POD and KRR-POD, are superior to those by the linear estimations LSE-POD and PCR-POD. In particular, the QSE-POD estimation could accurately reconstruct the temporal POD coefficients, as confirmed by its very high correlation coefficient in fig. 10b.

However, when we consider the performance of these estimation techniques for prediction, i.e. set 2, $time/\triangle t > 1050$, in the full domain (fig. 8), QSE-POD technique suffers a problem associated with overfitting. Overfitting refers to a situation in which model parameters respond to random fluctuations in the training data, thus reducing the reconstruction error but making the prediction worse [27]. This phenomenon makes the QSE-POD estimation model overly dependent on the individual wall gradient events, which in experiments includes both physical randomness and measurement noise. To reduce the dependence of model on large thus degrades amplitude fluctuations, an additional term, parameter β in KRR-POD is added to penalize the large weights in the model. Now for the wall domain, fig. 9a-d

Copyright © 2010 by ASME

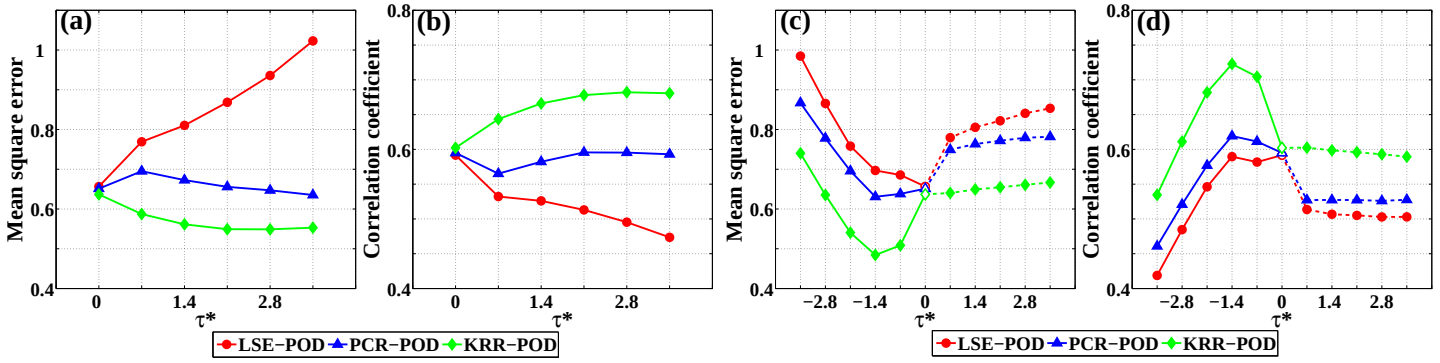

FIGURE 12. WALL DOMAIN: MULTI-TIME LSE-POD, PCR-POD AND KRR-POD, (a) MEAN-SQUARE ERRORS, (b) CORRELATION COEFFICIENTS BY USING BOTH OF THE PAST AND FUTURE INFORMATION OF WALL GRADIENTS, (c) MEAN-SQUARE ERRORS, (d) CORRELATION COEFFICIENTS BY USING THE PAST INFORMATION (SOLID) AND THE FUTURE INFORMATION (DASHED) OF WALL GRADIENTS.

compare the actual POD coefficients calculated from the original velocity fields with those from the estimation models. Figure 9e-h show the corresponding mean-square errors and correlation coefficients calculated for modes 1 and 4. One can clearly observe from fig. 9a-d that the estimation models perform well, as confirmed by the mean-square error and correlation coefficient shown by fig. 10c and d. It can be seen that the predictions of QSE-POD are less accurate than those of LSE-POD, PCR-POD and KRR-POD estimations, whose accuracies are extremely comparable.

Performance of multi-time LSE-POD, PCR-POD and KRR-POD estimations

In addition to the single-time estimations, we evaluate the performances of the multi-time LSE-POD, PCR-POD and KRR-POD estimations in predicting the POD coefficients of the velocity fields that are taken from the wall domain of the data set 2. The duration T into the past and/or future is a multiple of the PIV sampling interval, $T = I\Delta t$. Given the mean bulk velocity, U_m, and the step height h of the BFS flow, the non-dimensional duration τ^* is given by

$$\tau^* = \frac{TU_m}{h}. \tag{38}$$

It is important to note that for each duration T, the estimation coefficients of LSE-POD, PCR-POD and KRR-POD are recalculated, and the number N_p of "latent variables" of PCR-POD and the parameters (ε, β) of KRR-POD are re-optimized.

Figure 12a, b show the performances of the multi-time estimations LSE-POD, PCR-POD and KRR-POD in which both the past and future information of the wall gradient events are used. In this circumstance, the multi-time estimation LSE-POD corresponds to the estimation technique proposed by Durgesh and Naughton [10]. The results of single-time estimations shown in fig. 10c, d correspond to the case $\tau^* = 0$. An increase in duration τ^* reduces the accuracy of the multi-time LSE-POD prediction, while $\tau^* = 2.1$ yields only a slightly higher correlation coefficient than $\tau^* = 0$ for the multi-time PCR-POD estimation. By contrast, the performance of multi-time KRR-POD estimation in predicting the POD coefficients of velocity fields is best at $\tau^* = 2.8$.

Figure 12c, d show the mean-square errors and correlation coefficients obtained by the multi-time estimation techniques in which the information from the past and the future of wall gradient events is used separately. It can be seen that in our application, use of future information on wall gradient events reduces the accuracy of prediction of all the estimation techniques. On the contrary, using past information with $\tau^* = -1.4$ $(I = -2)$ yields the best prediction for PCR-POD and KRR-POD, minimizing mean-square error and maximizing correlation coefficient, though it does not improve prediction for the LSE-POD estimation. This result reasonably suggests a phase relationship between the wall gradient events and POD coefficients of the velocity fields of wall domain. The multi-time LSE-POD yields a worse prediction because it suffers from the problem of multicollinearity. Multicollinearity refers to the phenomena that the training data are statistically similar or correlated and hence close to linearly dependent [8]). Apparently, adding past and/or future information on wall gradients to the estimation models increases the linear dependence between individual wall gradient events. As built from linearly dependent data, the LSE-POD estimation invariably becomes sensitive to small changes in input information, while the KRR-POD estimations can handle collinear data [8]. From fig. 12, it can be observed that the nonlinear multi-time estimation, KRR-POD, performs best in predicting the POD coefficients of velocity fields if a certain duration of past information on wall gradient events is included in the model. This per-

Copyright © 2010 by ASME

formance demonstrates the capability of multi-time KRR-POD estimation to successfully capture the relationship between the POD coefficients and wall gradient events while PCR-POD is somewhat less successful. Note that the accuracy of prediction of multi-time estimations does not continue to increase beyond a certain value of T, which would limit its specification in practical application.

CONCLUSIONS

Considering to estimation models for real-time flow estimation, we have applied various estimation techniques to PIV experiments of turbulent flow over the backward-facing step. We have applied the snapshot POD to the three-component PIV velocity fields to calculate POD basis functions and their temporal coefficients. The low-order POD coefficients and the wall gradients measured by stereo interfacial PIV have been used to build POD-based estimation models, LSE-POD, QSE-POD, PCR-POD and KRR-POD, to estimate the low-order temporal POD coefficients of velocity fields.

In the first part, we have evaluated the performances of the single-time estimations LSE-POD, QSE-POD, PCR-POD and KRR-POD. The single-time estimation approaches build the estimation models by using the wall gradient information only at the instance when the estimation is performed. In this assessment, the QSE-POD estimation suffered from overfitting, which degraded its prediction, while the overall performances of the LSE-POD, PCR-POD and KRR-POD estimations are almost identical. Based on the performance and capability of single-time linear estimations, LSE-POD and PCR-POD in this application, the PCR-POD estimation is superior because it provides an optimal use of given events to achieve a better prediction, which is very useful for real-time flow estimation using sparse measurements.

When there is a time-lag between the POD coefficients and given events, it is more efficient to employ multi-time estimations. We have introduced the multi-time estimations PCR-POD and KRR-POD, which used the past and future information on wall gradients, to predict the POD temporal coefficients. The multi-time estimations require greater computational time in comparison to the single-time approaches. Compared to the multi-time LSE-POD estimation proposed by Durgesh and Naughton [10], our proposed multi-time estimations PCR-POD and KRR-POD yield more accurate prediction. Especially, the nonlinear multi-time KRR-POD estimation has successfully captured the structures of the flow given a certain past information on wall gradient events. This result indicated a phase relationship between the wall gradient events and POD coefficients of the velocity fields of wall domain. Implemented in the time-domain, the multi-time KRR-POD estimation does not need the Fourier transform of the measurement events as required in the frequency-domain approach proposed by Ewing and Citriniti [25]. As a result, after the estimation coefficients are determined, the multi-time KRR-POD may perform faster. In addition to having number of estimation coefficients constant with different values of duration τ^*, the multi-time KRR-POD estimation can handle collinear data and achieve the highest accuracy of prediction after a certain duration. For real-time estimation applications, it is only feasible to use the past information on the wall gradient events, i.e. $\tau^* \leq 0$, to build the estimation models.

Given that these results were obtained from the experimental data in a complex, three-dimensional recirculating flow, we suggest that the KRR-POD multi-time approach is a practically useful and that it may improve the capability for real-time estimation as compared with previous approaches.

ACKNOWLEDGMENT

This work has been supported by Research Fund for Accelerating International Research Activities 2009 at Ritsumeikan University. The first two authors are grateful for support from the Department of Mechanical, Materials and Aerospace Engineering of Illinois Institute of Technology, United States. The first author is grateful for a scholarship from the Japanese government (MEXT) during his studies.

REFERENCES

[1] Grant, I., Owens, E., Yan, Y., and Shen, X., 1992. "Particle image velocimetry measurements of the separated flow behind a rearward facing step". *Experiments in Fluids*, ***12***(4), pp. 238–244.

[2] Huang, H., 1994. "Limitations of and improvements to piv and its application to a backward facing step flow". PhD thesis, University of Technology Berlin.

[3] Kostas, J., 2002. "An experimental investigation of the structure of a turbulent backward facing step flow". PhD thesis, Monash University Melbourne.

[4] Naguib, A., Wark, C., and Juckenhofel, O., 2001. "Stochastic estimation and flow sources associated with surface pressure events in a turbulent boundary layer". *Physics of Fluids*, ***13***, pp. 2611–2626.

[5] Taylor, J., and Glauser, M., 2004. "Towards practical flow sensing and control via pod and lse based low-dimensional tools". *Journal of Fluids Engineering*, ***126***, pp. 337–345.

[6] Ukeiley, L., and Murray, N., 2005. "Velocity and surface pressure measurements in an open cavity". *Experiments in Fluids*, ***38***(5), pp. 656–671.

[7] Hudy, L., Naguib, A., and Humphreys, W., 2007. "Stochastic estimation of a separated-flow field using wall-pressure-array measurements". *Physics of Fluids*, ***19***, pp. 024103–024103.

[8] Mokhasi, P., Rempfer, D., and Kandala, S., 2009. "Predictive flow-field estimation". *Physica D: Nonlinear Phenomena*, ***238***(3), pp. 290–308.

Copyright © 2010 by ASME

[9] Cole, D., Glauser, M., and Guezennec, Y., 1992. "An application of the stochastic estimation to the jet mixing layer". *Physics of Fluids A: Fluid Dynamics,* ***4***, pp. 192–194.

[10] Durgesh, V., and Naughton, J., 2010. "Multi-time-delay lse-pod complementary approach applied to unsteady high-reynolds-number near wake flow". *Experiments in Fluids*, pp. 1–13.

[11] Nguyen, T., Wells, J., and Nguyen, C., 2010. "Wall shear stress measurement of near-wall flow over inclined and curved boundaries by stereo interfacial particle image velocimetry". *International Journal of Heat and Fluid Flow,* ***31***(3), pp. 442–449.

[12] Huang, H., Fiedler, H., and Wang, J., 1993. "Limitation and improvement of piv". *Experiments in fluids,* ***15***(4), pp. 263–273.

[13] Epps, B., and Techet, A., 2010. "An error threshold criterion for singular value decomposition modes extracted from piv data". *Experiments in Fluids,* ***48***(2), pp. 355–367.

[14] Lumley, J., 1967. "The structure of inhomogeneous turbulent flows". *Atmospheric turbulence and radio wave propagation*, pp. 166–178.

[15] Berkooz, G., Holmes, P., and Lumley, J., 1993. "The proper orthogonal decomposition in the analysis of turbulent flows". *Annual Review of Fluid Mechanics,* ***25***(1), pp. 539–575.

[16] Holmes, P., Berkooz, G., and Lumley, J., 1996. *Turbulence, coherent structures, dynamical systems and symmetry*.

[17] Sirovich, L., and Kirby, M., 1987. "Low-dimensional procedure for the characterization of human faces". *Journal of the Optical Society of America A,* ***4***(3), pp. 519–524.

[18] Kostas, J., Soria, J., and Chong, M., 2005. "A comparison between snapshot pod analysis of piv velocity and vorticity data". *Experiments in Fluids,* ***38***(2), pp. 146–160.

[19] Raffel, M., Willert, C., Wereley, S., and Kompenhans, J., 2007. *Particle Image Velocimetry: a Practical Guide*. Springer Verlag.

[20] Ma, X., Karniadakis, G., Park, H., and Gharib, M., 2003. "Dpiv-driven flow simulation: a new computational paradigm". *Proceedings of the Royal Society of London. Series A: Mathematical, Physical and Engineering Sciences,* ***459***(2031), pp. 547–565.

[21] Podvin, B., and Lumley, J., 1998. "Reconstructing the flow in the wall region from wall sensors". *Physics of Fluids,* ***10***, pp. 1182–1190.

[22] Adrian, R., 1977. "On the role of conditional averages in turbulence theory". In Conference on Turbulence in Liquids, Princeton, Science Press, pp. 323–332.

[23] Adrian, R., Jones, B., Chung, M., Hassan, Y., Nithianandan, C., and Tung, A., 1989. "Approximation of turbulent conditional averages by stochastic estimation". *Physics of Fluids A: Fluid Dynamics,* ***1***, pp. 992–998.

[24] Guezennec, Y., 1989. "Stochastic estimation of coherent structures in turbulent boundary layers". *Physics of Fluids A: Fluid Dynamics,* ***1***, pp. 1054–1060.

[25] Ewing, D., and Citriniti, J., 1999. "Examination of a lse/pod complementary technique using single and multi-time information in the axisymmetric shear layer". *Fluid Mechanics and its Applications,* ***52***, pp. 375–384.

[26] Tinney, C., Coiffet, F., Delville, J., Hall, A., Jordan, P., and Glauser, M., 2006. "On spectral linear stochastic estimation". *Experiments in Fluids,* ***41***(5), pp. 763–775.

[27] Hawkins, D., 2004. "The problem of overfitting". *J. Chem. Inf. Comput. Sci,* ***44***(1), pp. 1–12.

Copyright © 2010 by ASME